The International Journal of Advanced Manufacturing Technology (2021) 116:1881–1893
https://doi.org/10.1007/s00170-021-07515-3

ORIGINAL ARTICLE

Influence of isothermal aging in LDX 2101 duplex stainless steel on the microstructure and local properties

Naima Ouali[1] · Billel Cheniti[1] · Brahim Belkessa[1] · Bouzid Maamache[1] · Ramdhane Kouba[2] · Maamar Hakem[1]

Received: 9 April 2021 / Accepted: 17 June 2021 / Published online: 5 July 2021

Abstract

In the present work, the interface morphology and the evolution of nitride precipitates in LDX 2101 stainless steel isothermally treated at 750 °C for various aging times were investigated. The microstructure results showed that the Cr_2N nitrides precipitated along the δ/γ interface with 200 nm in length and continue to grow to 2 μm after 240 h of aging. However, only Cr_2N nitrides were found at the δ/δ interface after long term of aging. Atomic force microscopy (AFM) analysis revealed that Cr_2N nitrides and $Cr_{23}C_6$ carbides started to precipitate after the first 10 min of aging with a small needle shape of the former and specific triangular morphology of the latter. The evolution of hardness and Young's modulus of the interfaces, performed with nano-indentation measurements, showed that the δ/γ interface became harder (4.1 ± 0.2 GPa) with increasing aging times, whereas negligible changes in the hardness and elastic modulus were recorded at the δ/δ interface. 3D topographic analysis of the immersed surfaces revealed that the susceptibility of δ phase to preferential dissolution in 3.5% NaCl solution increased with aging time. This behavior was manifested by the important imperfections of δ phase, the high surface roughness (55.7 nm), and the deep corrosion pits (30 nm) along the δ/γ interface and around the Cr_2N nitrides.

Keywords Microstructure · Interface · Precipitates · Nano-hardness · Surface degradation

1 Introduction

The low cost and decent stability of the ferrite (δ) and austenite (γ) phases in lean duplex stainless steels (LDXs) have raised much interest in the last two decades [1]. The LDX 2101 grade has known a boosting demand as a result of its increased application in steam generators and pressure vessel, thanks to the lightened range in nickel element without altering the phases balanced, the excellent mechanical properties, and high corrosion resistance [2, 3]. It is known that the good properties of LDX steel may be affected when the steel is exposed to high-temperature treatment that results in phase decomposition and precipitation of undesirable phases [4–6].

✉ Brahim Belkessa
brbelkessa@yahoo.fr

[1] Research Center in Industrial Technologies CRTI, P.O. Box 64, Chéraga, Algeria

[2] Laboratoire de Technologie des Matériaux, Département SDM, Faculté de Génie Mécanique et Génie des Procédés, USTHB, BP 32 El-Alia, 16111 Algiers, Algeria

Indeed, the high sensitivity of LDX 2101 to the nitride precipitation, as a substantial fraction of nitrogen, presents a critical issue as sigma phase precipitation in 2205 DSS, which affects the toughness and the corrosion resistance of the steel [6, 7]. The aging treatment of LDX 2101 at 700 °C produces intermetallic precipitates along the δ/γ and δ/δ boundaries and a secondary austenite phase (γ_2), with low-chromium concentration in the neighboring formed precipitates [8]. The ferrite phase decomposition according to the eutectoid transformation ($\delta \rightarrow Cr_2N + \gamma_2$ and $\delta \rightarrow M_{23}C_6 + \gamma_2$) resulted in nitride, carbide, and γ_2 formation especially at the δ/γ interfaces [9]. The transformation kinetic of the above eutectoid reaction is strongly related to temperature range and exposure time. The embrittlement nose of nitride precipitation in LDX 2101 is roughly situated between 650 and 750 °C where the maximum amount of Cr_2N is reached at 700 °C. It is assumed that the low Mo content and the high amount of N as alloying elements in the LDX 2101 steel favor the Cr_2N precipitation instead of sigma phase when the steel is subjected to heat treatments. Meantime, Cr_2N nitrides were found in 2205 stainless steel after a long aging treatment between 700 and 900 °C and rapid cooling [10]. Numerous research works have reported the negative effect of chromium nitride precipitation on the

microstructure and mechanical behavior of welded or isothermally heat-treated DSS [11–16]. It is found that Cr_2N precipitated at δ/γ boundaries in 2507 super duplex stainless steel after 3-min holding time at 900 °C while these precipitates were formed within δ grains at 850 °C after 3-min aging temperature [17, 18]. This resulted in a decrease in impact energy, an increase in hardness and the wear resistance of the aged samples with remarkable microstructural changes along the interfaces [19, 20]. In other research works, Cr_2N precipitates were detected at δ/γ and δ/δ interfaces and in the ferrite phase after isothermal aging at 700–900 °C without formation of sigma and chi phases in LDX 2101, which directly affect the electrochemical behavior of the studied steel [21–24]. Deng et al. [23] found that the corrosion resistance of δ decreases due to the creation of the Cr-Mo depletion zone at the vicinity of δ grain boundaries. In fact, the chromium depletion zone that resulted from the eutectoid decomposition of ferrite phase is highly susceptible to dissolution that implies high pitting corrosion rate [21, 25]. At high temperature, δ phase decomposition raises the formation of Cr_2N and secondary phases that promotes pitting corrosion occurrence at/or adjacent to the formed precipitates [21]. Perren et al. [26] found that Cr_2N nitrides decrease significantly the corrosion resistance and the passivation behavior of the DSS. However, Ha et al. [27] concluded that the lamellar Cr_2N was the most susceptible site for corrosion compared to the ones precipitated along the grain boundaries. The literature reported limited research works that correlate the nitride morphologies to their effect on the corrosion response of the isothermally aged LDX 2101 steel. Therefore, in the present work, close examination of the effect of nitride precipitates on the evolution of phase interfaces in LDX 2101 stainless steel aged at 750 °C for several aging times is conducted. The influence of Cr_2N nitride morphology and secondary phases on the microstructure, local mechanical properties (hardness and elastic modulus) using nano-indentation measurements of the treated steel is deeply investigated. Furthermore, immersion tests in the chloride environment are performed to evaluate the surface imperfections of the aged specimens and highlighted the precipitates' role on the degradation degree of the immersed surfaces

2 Materials and experimental procedures

The investigated material used in this work is a lean duplex stainless steel LDX 2101 (UNS S32101), received in a plate form of 6.5-mm thickness and dimensions of 50 × 50 mm^2, with the chemical composition given in Table 1. Specimens with a 20 × 20 mm^2 square surface were cut from the received plate and solution-annealed at 1050 °C for 60 min, followed by water quenching. Thereafter, the specimens were isothermally aged at 750 °C for different holding times (10 min, 20 min, 1 h, 10 h, 24 h, 72 h, 120 h, and 240 h) and water quenched to produce microstructural changes (precipitates and secondary phases) that could influence the interfacial behavior between phases.

The obtained samples were prepared for optical metallography and electrolytically etched using a LectroPol-5 machine with 1 M KOH solution working at 5 V for 6 s. The microstructural examination of the samples was conducted using a Nikon optical microscope and a ZEISS Gemini SEM 300 scanning electron microscope (SEM) equipped with an energy-dispersive spectroscopy (EDS) detector for the chemical analysis of the different constituents.

X-ray diffraction (XRD) analysis was performed to identify the phases of the aged samples using Bruker D2 Phaser 2^{nd} generation with Cu (Ka) radiation (0.15406 nm) operating at 40 kV and 40 mA, with the parameters of angular interval 2θ: 10–120°, angular step: 0.026°, and 72-s time per step. The obtained patterns were characterized by HighScore software using the PDF4 database.

Global mechanical behavior of the aged samples has been conducted by hardness measurements using a Buehler WILSON VH3300 hardness machine under 10 kg/f load and 10-s dwell time. The local mechanical properties of the different phases were evaluated through nano-indentation measurements using an Anton-Paar NHT-3 nano-indenter with a Berkovich tip under a 10-mN applied load. Five indents were conducted in the ferrite phase, austenite phase, δ/γ interface, and δ/δ interface in order to obtain an average value of hardness (H_{IT}) and Young's modulus (E_{IT}) of each region using the Oliver and Pharr method [28].

The corrosion behavior of the specimens was evaluated by the immersion test into 3.5% NaCl solution for 72 h at room temperature. Before and after immersion tests, the surface observations of the aged specimens were performed by atomic force microscopy (AFM) using ScanAsyst, Bruker instrument, working in PeackForce tapping mode. To carry out the different measurements, magnetic force microscopy (MFM) mode was employed to identify the magnetic behavior of different phases. The topographic images of the samples were generated during the first scan whereas the magnetic

Table 1 Chemical composition of the LDX 2101

Element	C	Si	Mn	P	S	Cr	Ni	Mo	N	Fe
wt.%	0.03	0.7	4.72	0.025	0.01	21.2	1.74	0.29	0.25	Bal.

response of the scanned surface was obtained with a lift of 118 nm between the sample surface and the MESP tip, taking into consideration the topography recorded during the first pass. All the images were processed with the Nanoscope V from Veeco Instruments Inc., where the surface roughness and pit depth were examined.

3 Results and discussion

3.1 Evolution of precipitate morphology and interfaces with aging time

Figure 1a shows the optical micrograph of the as-annealed sample treated at 1050 °C for 60 min. A typical equilibrium microstructure of bright γ-austenite phase is distributed in a dark matrix of δ-ferrite with average amounts of 48% and 52%, respectively. It can be seen, from the AFM image of the as-annealed sample shown in Fig. 1b, the smooth aspect of γ compared to that of δ phase with 6-nm and 13-nm roughness, respectively. The γ/δ interface illustrated in Fig. 1c obtained using MFM mode exhibits a precipitation-free interface with no secondary phases throughout the interface where striped magnetic domains of the ferromagnetic δ phase with high contrast but not in the paramagnetic γ-austenite are clearly seen.

Figure 2a–d shows the microstructure evolution of the LDX 2101 samples aged at 750 °C for 10 min, 1 h, 24 h, and 240 h, respectively. After 10 min of aging (Fig. 2a), tiny black dots (precipitates) are observed at the γ/δ interfaces surrounded by white pancake-like structure so-called secondary austenite (γ_2). Increasing the aging time to 1 h (Fig. 2b), the precipitates became more pronounced and their amounts increase progressively at the γ/δ interface into the detriment of δ phase (Fig. 2c and d after 24-h and 240-h aging time, respectively). These phases appeared as consequence of the eutectoid transformation of δ phase into nitrides and carbides (δ.→ γ_2+ M_2N+ $M_{23}C_6$). Numerous research works [1, 19, 29] reported that, in LDX 2101, nitrides start to nucleate in the earliest stages of aging (after the first 6 min) at 750 °C along ferrite/austenite grain boundaries. Maetz et al. [8] mentioned that due to the low C content in LDX 2101 steel (<0.03 wt.%), the $M_{23}C_6$ carbides stop to nucleate after the first 15 min of aging, whereas M_2N nitrides continue to grow along the γ/δ interface and start to precipitate at the δ/δ interface with longer aging times. According to the Thermo-Calc diagram (using the TCFE7 database) illustrated in Fig. 3a, below 760 °C, secondary phases, i.e., nitrides, carbides, and sigma phase, are formed where the highest molar fraction of nitrides of about ~4% is precipitated at 750 °C and that to the detriment of ferrite phase (around 38%). This behavior is discriminated from meaning values due to the hors-thermodynamic equilibrium conditions in which the steel is treated [30]. Simultaneously, small fraction of carbide precipitates (0.5%) is formed where the δ-ferrite seems to be instable around this temperature. On the other side, γ phase exhibits a slight increase in molar fraction, which is more likely attributed to the formation of γ_2-secondary austenite. The XRD patterns shown in Fig. 3b–d confirm that the precipitates already formed are Cr_2N nitrides and $Cr_{23}C_6$ carbides with the absence of sigma phase. In the as-annealed specimen (Fig. 3b), only δ and γ phases are identified with intense peaks. After 1 h of aging, a remarkable decrease in ferrite intensity peak is obtained (Fig. 3c) that becomes barely detected after 240-h aging time (Fig. 3d). Meantime, Cr_2N exhibits intense peak as aging time increases. The high peak intensity of Cr_2N reflects the increase of its content as aging time increases suggesting the important decomposition of δ-ferrite into Cr_2N and $Cr_{23}C_6$ precipitates.

The EDS elemental mapping analysis conducted at a triple junction of the sample subjected to 24 h of aging is shown in Fig. 4. It can be seen from the superposition of Cr and N elements that the precipitates formed at the interface are essentially chromium-rich nitrides where secondary austenite

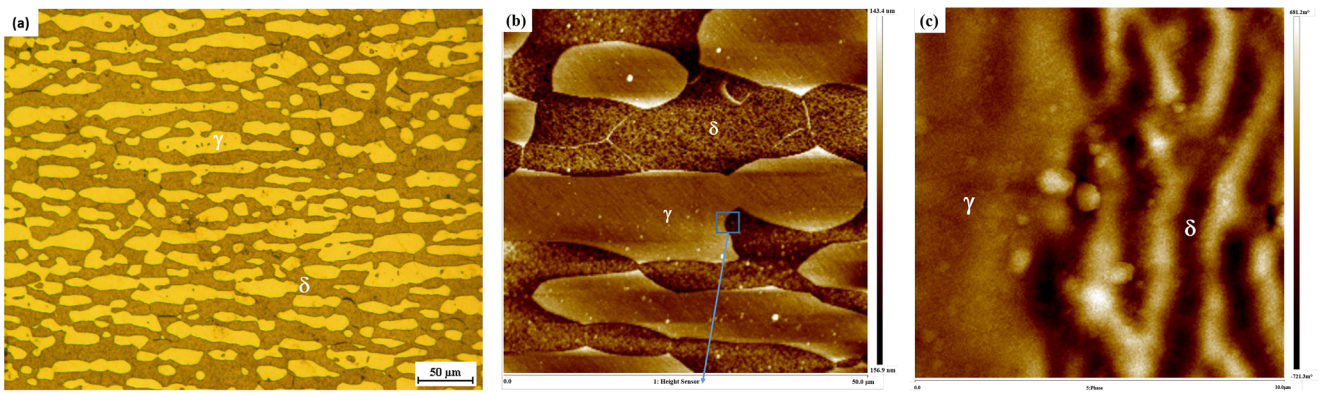

Fig. 1 Microstructure of the as-annealed LDX 2101 sample. **a** Optical micrograph. **b** AFM image of the as-annealed structure. **c** Zoom view of the δ / γ interface using MFM mode

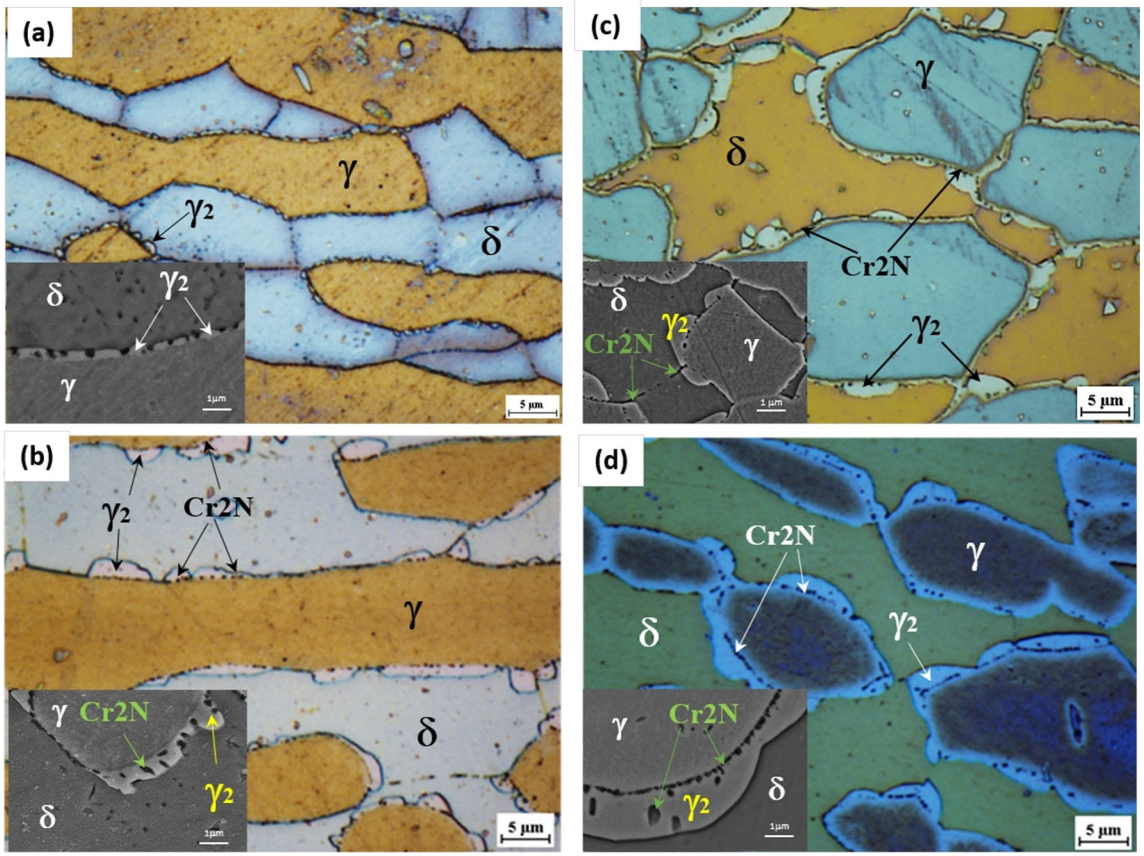

Fig. 2 Optical and SE-SEM micrographs of lean duplex aged at 750 °C for **a** 10 min, **b** 1h, **c** 24 h, and **d** 240 h

can be distinguished from the chromium depletion region with dark contrast around the bright precipitate. The semi-quantitative EDS microanalysis conducted in this region illustrated in Table 2 reveals clearly that the secondary austenite contains less chromium compared to the primary austenite (16 wt.% and 20 wt.%, respectively). On the other side, at the γ/precipitate interface, a high level of N and Cr elements is recorded (15 wt.% and 26 wt.%, respectively), which confirms the presence of Cr_2N nitrides. It is believed that the high stacking fault energy of δ phase compared to γ and the rapid diffusion kinetics within δ structure facilitate the Cr, Mo, and N diffusion into the former phase due to the compact crystal structure of FCC compared to the BCC one. Furthermore, the interstitial solid solution of N, since its small atom size, and the high chemical affinity to Cr element favor the formation of chromium-nitride compounds in preferential sites with high stacking fault energy as grain boundaries or even inside the ferrite grain [31, 32]. Deng et al. [33] revealed the formation of small amount of σ phase adjacent to Cr_2N at 700 °C that increases in volume fraction with increasing aging time. However, in the present investigation, only the Cr-depleted region (γ_2) was observed at the surrounding of Cr_2N precipitates.

The evolution of the Cr_2N morphology with aging time is shown in Fig. 5a–d. As mentioned above, the precipitation mechanism of Cr_2N nitrides is the consequence of the eutectoid decomposition of ferrite. This mechanism is often the main factor responsible on the precipitate morphology [9]. It can be seen that after the first 10 min of aging (Fig. 5a), Cr_2N nitrides start to precipitate in a small needle shape of 200-nm length at the δ/γ grain boundary and grow towards the ferrite phase with further aging. The AFM image of the sample aged after 1 h reveals that these precipitates appear as small bright dots along δ/γ interfaces (Fig. 5e) where the ferromagnetic ferrite and the paramagnetic austenite are clearly observed (Fig. 5f). A significant Cr_2N growth is produced with a needle-like structure that reaches 1.5-µm length after 24 h of aging (Fig. 5c). Increase in aging time to 240 h results in increasing (2 µm) and dispersion of Cr_2N nitrides throughout the γ_2 matrix (Fig. 5d).

From the above images, it seems difficult to distinguish between nitride and carbide precipitates using SEM, even with high magnifications. The small size of $Cr_{23}C_6$ carbides, their formation at the earliest stages of aging treatment, and their identical appearance under a SE microscope (small black dots) require the employment of powerful investigation techniques that allow the visualization and the distinction between these

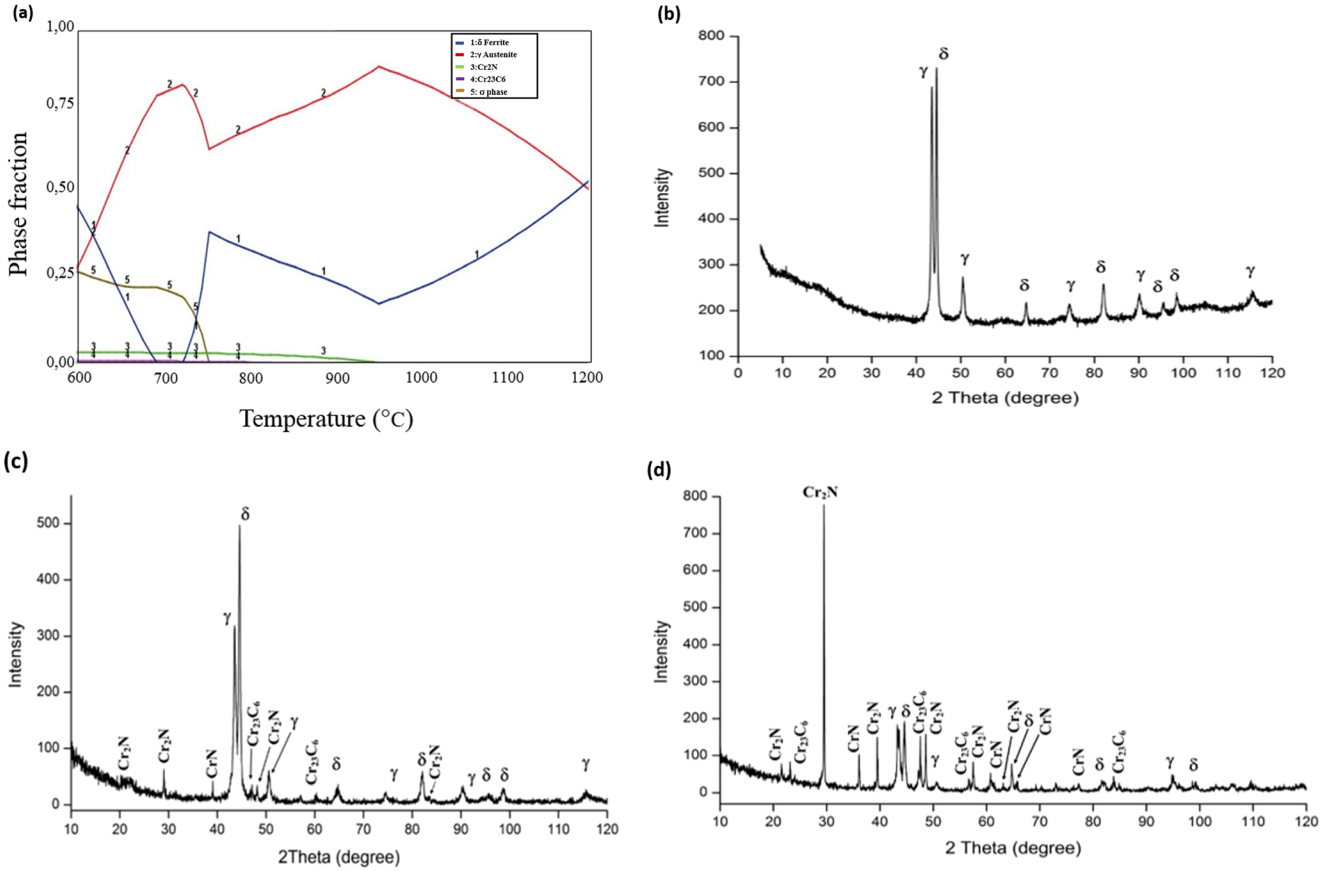

Fig. 3 **a** Thermo-Calc diagram of the phases present in the LDX 2101 after heat treatment and the XRD patterns of (**b**) as-received sample and (**c**, **d**) samples aged after 1-h and 240-h time, respectively

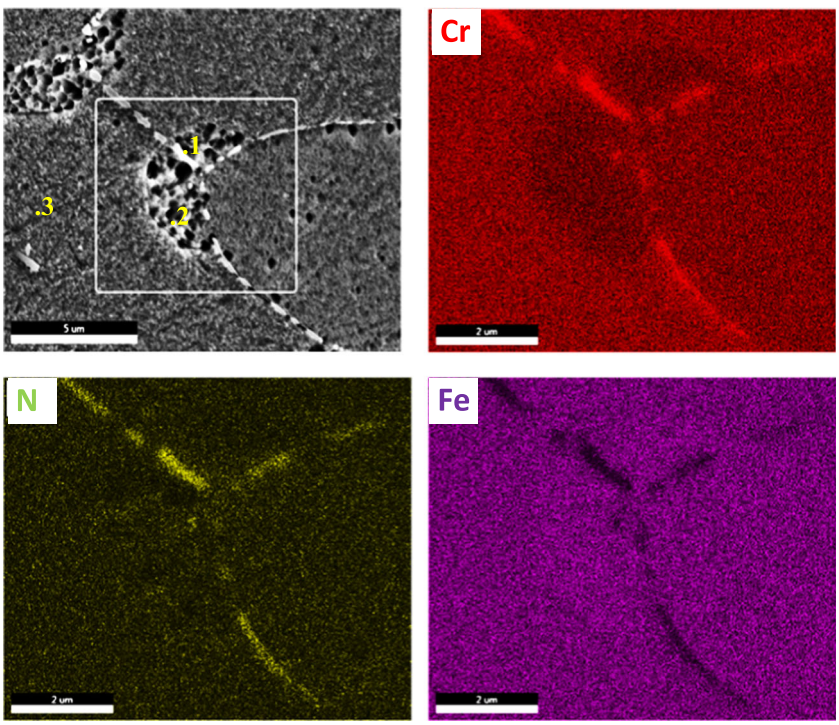

Fig. 4 SE-SEM image and EDS mapping analysis conducted at a triple junction of the sample aged for 24 h at 750 °C

Table 2 EDS point analysis conducted in the triple junction targeted in Fig. 4

Elements wt.%	Cr	Ni	N	Mn	Fe
.1	26.2	2.3	15.1	1.5	Bal.
.2	16.4	4.5	0.1	5.6	Bal.
.3	20.1	3.2	0.3	6.1	Bal.

precipitates. Maetz et al. [34] revealed, using TEM and FIB techniques, that the precipitate morphology depends on the grain boundary nature. They found that Cr_2N precipitated as a rod-like structure at γ/δ and δ/δ interfaces whereas triangle $Cr_{23}C_6$ carbides precipitate only at the γ/δ interface with no longer evolution with aging time. Figure 6a shows the AFM image, using tapping mode, of the sample isothermally treated after 10 min of aging. The δ phase is distinguished by a dark contrast while a brighter contrast of γ phase is observed. It is clear, from Fig. 6b, that the γ/δ interface is pinned by highly bright precipitates compared to both parent phases. The decomposition of δ-ferrite into secondary phases is highlighted by the heterogeneous contrast that resulted from its roughness and the formation of new precipitates. The scan of a small area of the γ/δ interface reveals the triangle shape of $Cr_{23}C_6$ carbides randomly distributed throughout the interface and into the γ_2 with 100–150-nm main size (Fig. 6b, c). Hang et al. [35] explained that the increase in misorientation between two adjacent grains (ferrite and austenite) allows the carbide growth through the lowest interfacial energy, which results in the triangular morphology of $C_{r23}C_6$ carbides. Brighter fine precipitates are also observed along the δ/γ interface and into the ferrite phase (Fig. 6c) that are attributed, according to their morphology, to Cr_2N nitrides (150 nm in length). These results are in good agreement with those found by previous research work [34]. The preferential nucleation and growth of precipitates towards δ phase results in δ/γ interface migration from the precipitate particles into δ phase (Fig. 7a–c), leaving the precipitates behind along the original interfaces, which increases the size of the secondary austenite. On the other side, no precipitates were detected at the δ/δ interface after aging up to 120 h. However, precipitates start to appear at the δ/δ interface in the sample aged for 240 h (Fig. 7b), which are more likely Cr_2N nitrides according to Maetz et al. [8], who demonstrated that only nitrides may be formed at this interface and that for a long aging treatment. It is interesting to note that on the MFM image of the sample aged at 240 h (Fig. 7c), the secondary austenite exhibits a ferromagnetic behavior contrary to the paramagnetic primary austenite. Silva et al. [36] established that $Cr_{23}C_6$ carbides are paramagnetic and the decrease in chromium content in austenitic stainless steel promotes the increase of Curie temperature over room temperature which results in the transformation of the paramagnetic austenite to the ferromagnetic structure as proposed by Stevens et al. [37].

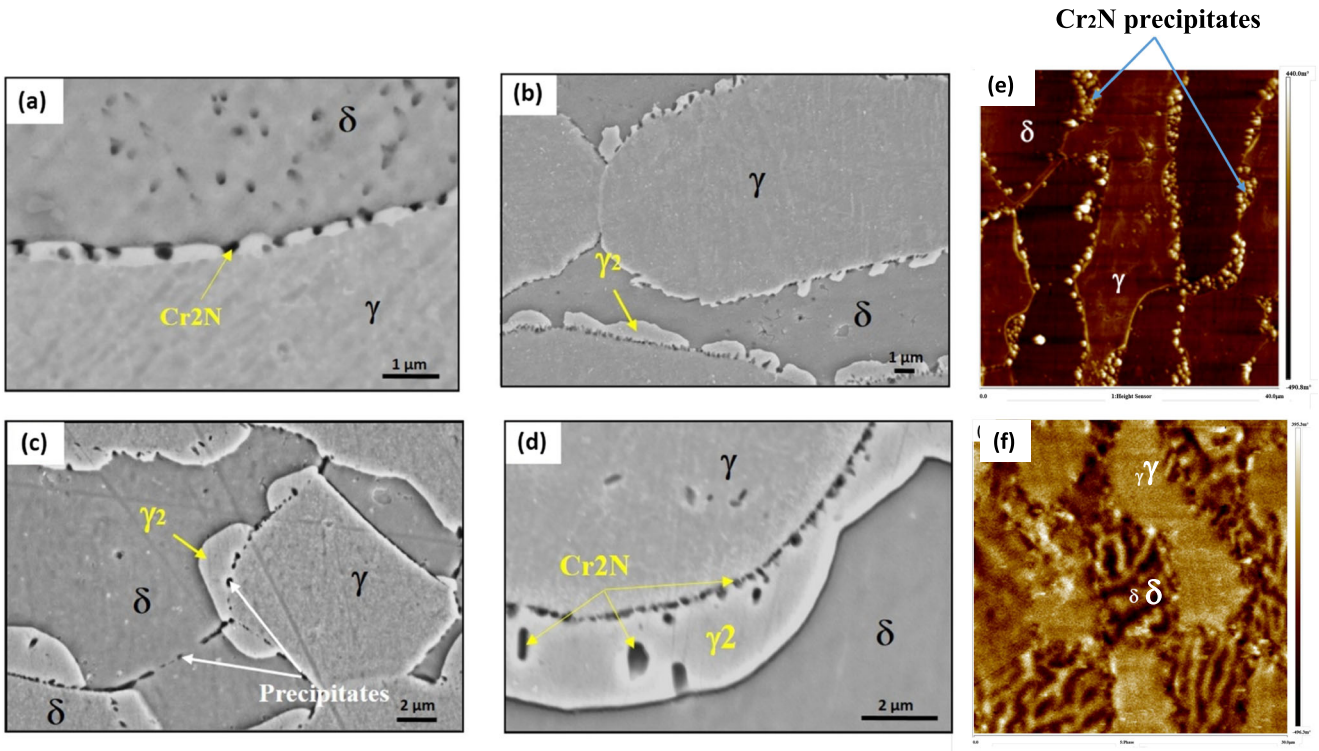

Fig. 5 δ / γ interface evolution and precipitation morphology with aging time. SE-SEM images (**a**) after 10-min aging, (**b**) after 1-h aging, (**c**) after 24-h aging, and (**d**) after 240-h aging. **e**, **f** AFM and MFM after 1-h aging time

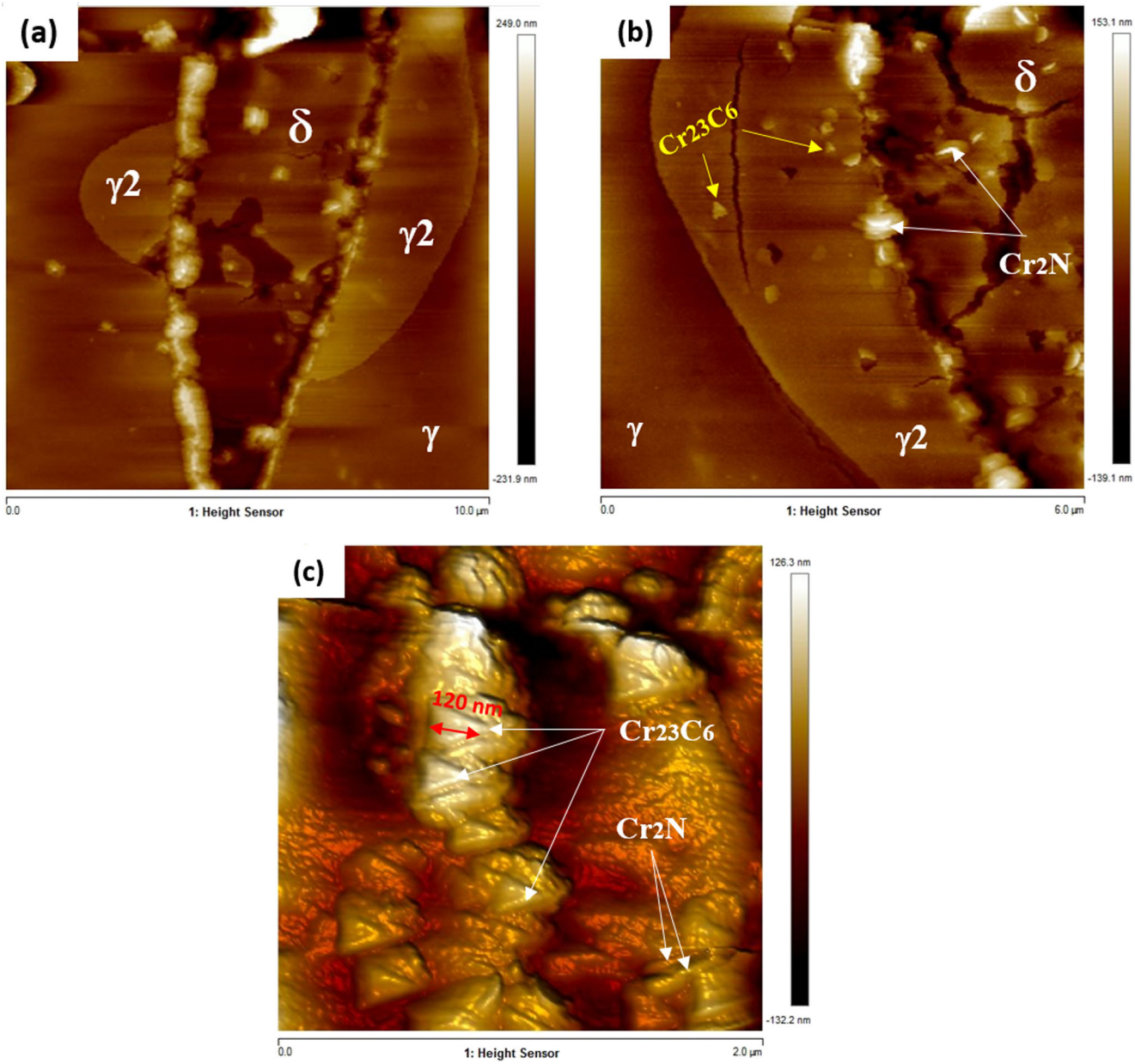

Fig. 6 **a** AFM image of the microstructure of the sample aged after 10 min. **b** Small scanned area of the δ / γ interface. **c** AFM image of $Cr_{23}C_6$ carbides with a triangular shape

3.2 Effect of aging time on the hardness

The hardness evolution of the as-annealed and the aged samples is exhibited in Fig. 8. A slight decrease in hardness values is recorded (from 235±4 HV10 to 225±3 HV10 for 10-min and 240-h aging times, respectively) with aging time. This behavior can be explained by the formation of Cr depletion zones, as a consequence of the eutectoid decomposition of ferrite, that increases with aging time. Similar results were found by Zhao et al. [38] who reported that for a long aging period, nitrogen element (austenite-stabilizing element) diffuses from the austenite phase matrix to form nitrides at the grain boundaries, which results in the decrease of hardness of the aged samples.

3.3 Local-mechanical behavior of interfaces after aging treatment

Figure 9a shows load-displacement curves with optical images incorporated in the same plot to confirm the position of the indents belongs to a specific phase. It is clear from the load segment that both phases exhibit different deformation behaviors. At low indentation depth (before 100 nm), ferrite displays distinct elastic regime whereas at greater depth, similar plastic trends were observed. As it can be seen, the austenite reaches a highest load at 225 nm than ferrite (300 nm), suggesting its high hardness (4.7 GPa and 3.1 GPa, respectively). The unload parts show a similar behavior implying the same

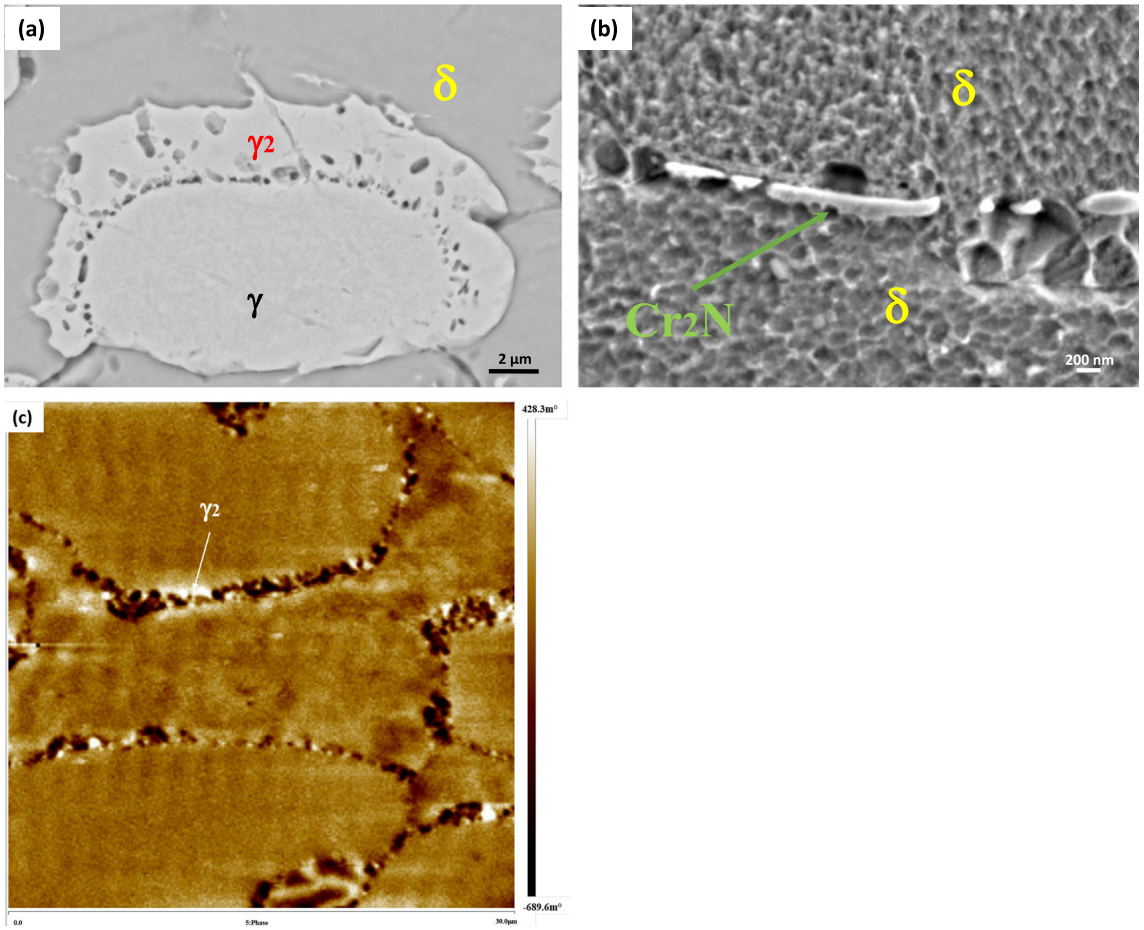

Fig. 7 Cr_2N precipitate and γ_2 morphology of the sample aged at 750 °C for 240 h. (**a**) BSE-SEM image and (**b**) SE-SEM image of the ferrite/ferrite interface with a needle-like structure of Cr_2N. (**c**) MFM image of the 240-h aged sample

stiffness and elastic modulus of both phases (around 241 GPa). It has been believed that in DSSs, the strength is enhanced by the hard ferrite, whereas the softening is insured by the austenite phase. However, the strengthening effect of N element and its high solubility in austenite phase are the main reason for the higher hardness of the latter compared to ferrite

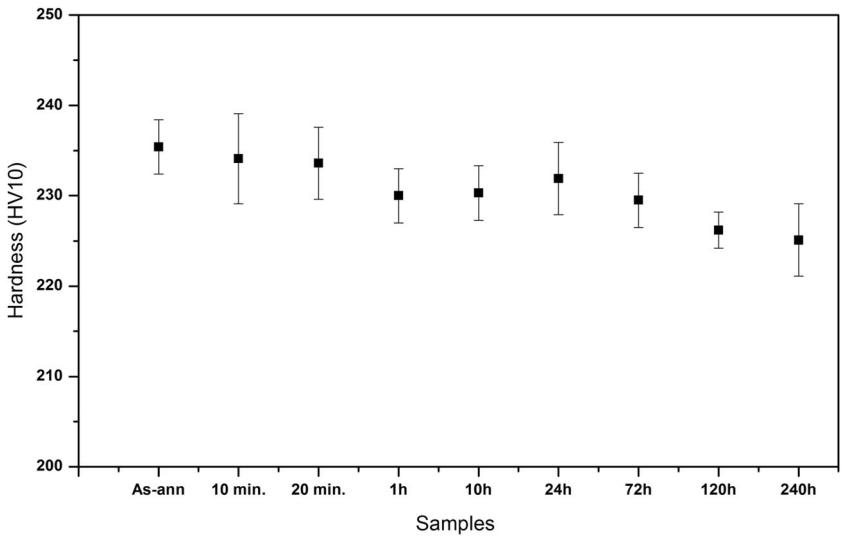

Fig. 8 Vickers hardness measurements

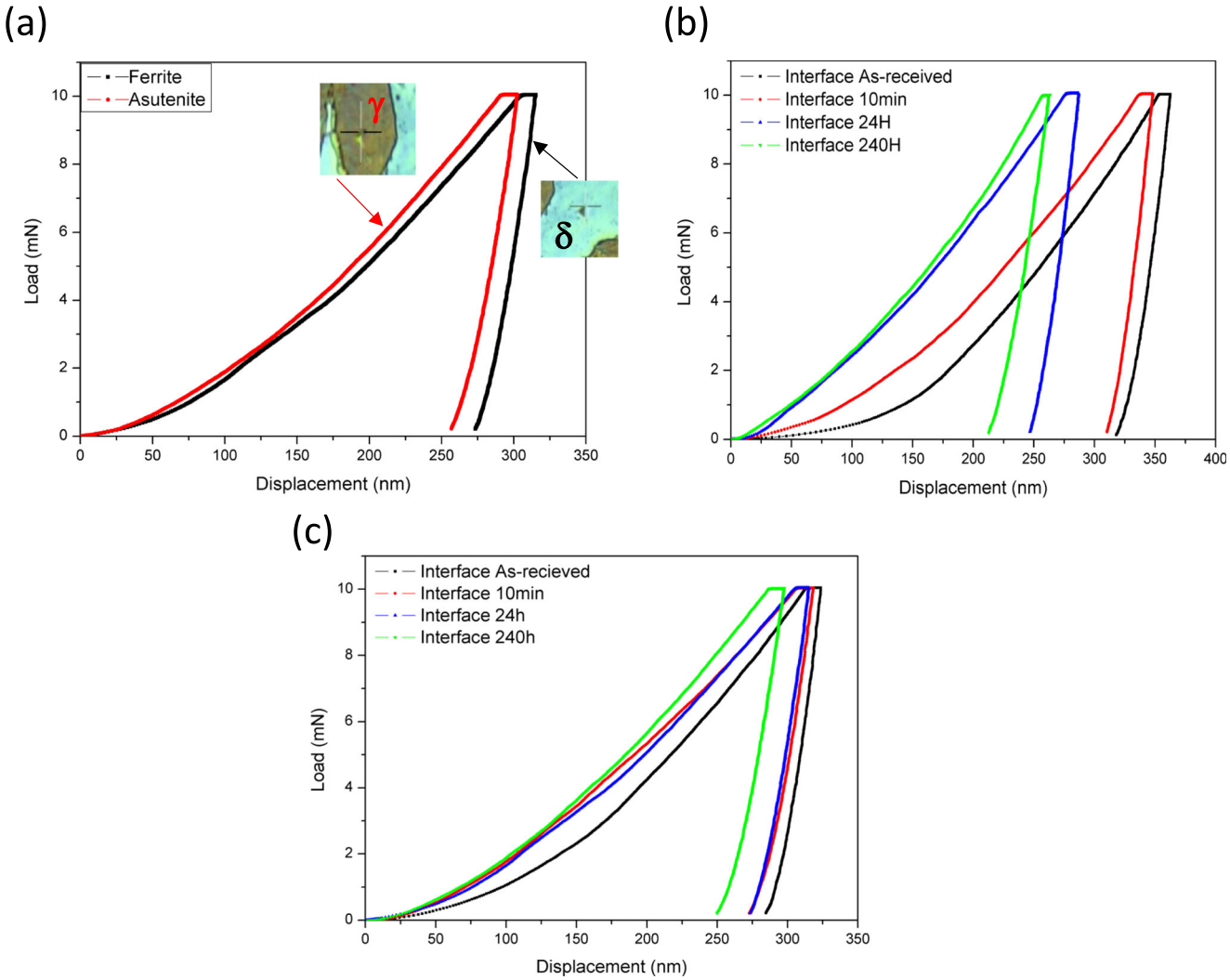

Fig. 9 Load-displacement curves of (**a**) γ and δ phases, (**b**) γ / δ interfaces, and (**c**) δ / δ interfaces of the samples aged at 750 °C for different times

phase [8]. Similar results were found by Fang et al. [39] who concluded that the austenite phase becomes harder when the nitrogen content in the steel is higher than 0.2%.

The calculated average hardness and indentation Young's modulus of interfaces issued from different aging times are illustrated in Table 3. The low scatter of the experimental data reflects the reliability of nano-hardness and indentation modulus measurements. Two distinguished domains can be observed from load-displacement curves of the aged δ/γ interfaces (Fig. 9b). Under the same applied load, the penetration depth was less with increased aging time (24 h and 240 h), while the as-annealed specimen and the sample aged at 10-min aging time exhibit roughly the similar tendency, suggesting that the interface resistance to penetration was higher at high aging time, which signifies the low hardness of the interfaces after low aging time (see Table 3). Meantime, the slopes of δ/δ interfaces illustrated in Fig. 9c seem to be unaffected by aging treatment indicating negligible changes in hardness (4.8 ±0.3 GPa) except after 240 h of aging (5.1 ±0.2 GPa). These results can be explained by the precipitation of Cr_2N at the δ/δ interface that takes place after a long time of aging.

Table 3 Nano-hardness (H_{IT}) and Young's modulus (E_{IT}) values measured in different phases and the δ/γ interface of the specimens aged for various times

	Ferrite	Austenite	As-annealed	10-min aging	24-h aging	240-h aging
H_{IT} (GPa)	3.1±0.3	4.7±0.2	3.4±0.1	3.7±0.5	3.9±0.4	4.1±0.2
E_{IT} (GPa)	234±7	249±8	241±5	245±6	249±5	247±4

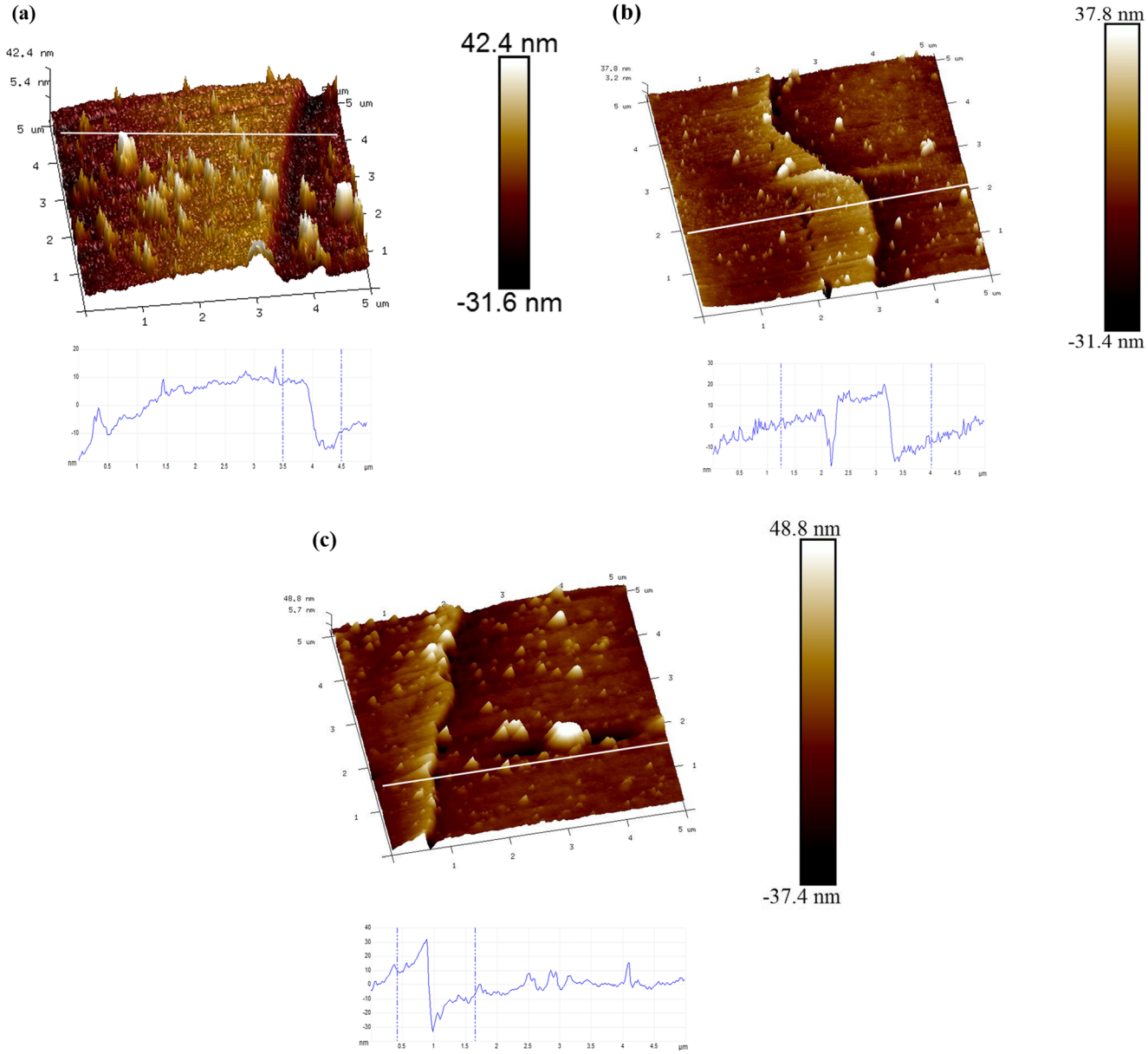

Fig. 10 3D AFM images of the surface topography with the corresponding line profiles after immersion in 3.5% NaCl solution for the (**a**) as-annealed sample, (**b**) 10-min aged sample, and (**c**) 240-h aged sample

3.4 Effect of secondary phases on the surface response of the aged samples

The surface imperfections of the aged specimens after immersion tests in 3.5% NaCl solution for 72 h are analyzed using AFM. 3D topographic images with the corresponding line profile of the as-annealed and isothermally aged samples at 10 min and 240 h after immersion tests are shown in Fig. 10a–c. It can be seen that on all sample surface, small white particles that are attributed to the Na and Cl (salt) stacked on the

Table 4 Roughness measurements in δ and γ phases after immersion tests in 3.5% NaCl of different aged samples

Samples	As-annealed		10-min aged sample		240-h aged sample	
Arithmetic roughness (Ra) nm	Ferrite (δ)	Austenite (γ)	Ferrite (δ)	Austenite (γ)	Ferrite (δ)	Austenite (γ)
	23.7	7.4	38.8	4.9	55.7	5.2

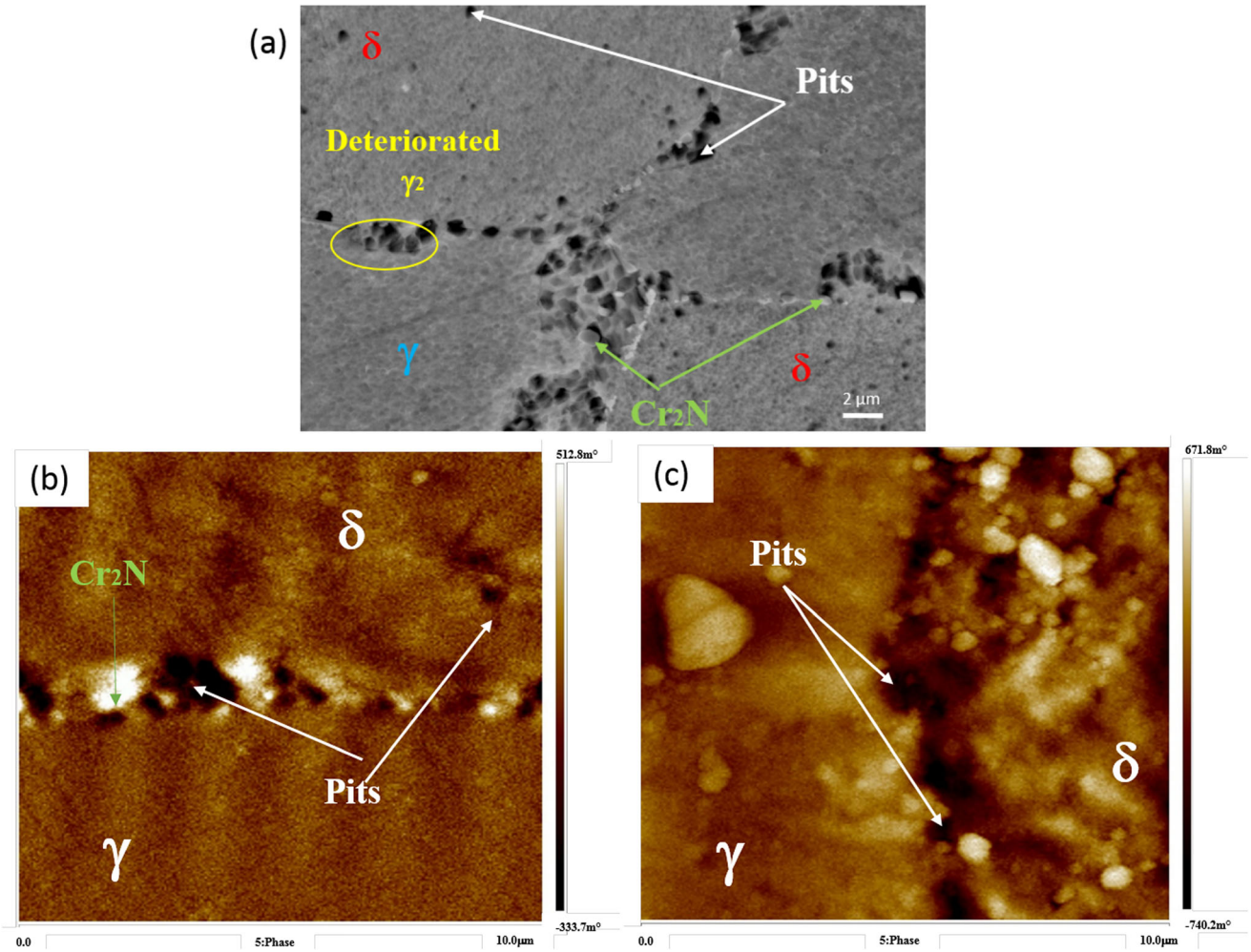

Fig. 11 Austenite/ferrite interface obtained after immersion tests. **a** BSE-SEM image of the sample aged after 24 h. **b**, **c** AFM images of the samples aged after 24 h and 240 h, respectively

surface holes and along the interfaces after both water cleaning and hot air drying. The as-annealed specimen exhibits a smooth surface with a main roughness value of about 18 nm. As seen in Fig. 10a, a heterogeneous distribution of roughness over the sample surface is observed where the δ phase shows the highest values of roughness compared to the γ phase one (Table 4). This indicates the high susceptibility of δ phase to the preferential dissolution in NaCl solution and its deterioration turned deeper with increasing aging time. A similar behavior was observed by Guat et al. [40] who found that the high content of nickel and nitrogen elements in austenite phase resulted in the lowest corrosion potential in ferrite phase in 2507 super duplex stainless steel. This phenomenon is explained by the low active status of alphagen-Cr element in hydroxide solution than that of gamagen-Ni element, which results in the best corrosion resistance of austenite phase. Except for the as-annealed specimen, the aged samples exhibit important changes in surface roughness. A uniform δ/γ interface is seen in the as-annealed specimen with shallow pits (12 nm in depth) throughout the ferrite surface and along the δ/γ interfaces. Meantime, the surface of the sample obtained after 10-min aging time (Fig. 10b) shows a homogeneous roughness pattern that is higher than the as-annealed one where important imperfections of δ phase with nitrides, uniformly distributed along the interface, are observed. The worst surface aspect is found in the specimen aged at 240 h subjected to the NaCl solution, which presents deep holes (pits of 30 nm in depth) and imperfection at the grain boundaries (Fig. 10c). It can be seen that after 10 min of aging, the surface exhibits pits at the vicinity of γ_2 and inside δ phase that become prominent after 240 h of aging. Furthermore, pits are detected around the Cr_2N (Fig. 11a, b) that become deeper with increasing aging times (Fig. 11c). The nucleation of pits and their growth through the interface and around the Cr_2N is attributed to the nature of elements present in each zone (phase). Furthermore, the low chromium content at the δ/γ interfaces, due to the formation of Cr_2N and $Cr_{23}C_6$ precipitates, promotes the nucleation of further preferential site for

pitting, exclusively in secondary austenite. Therefore, it can be said that the γ_2 phase acts as the origin of pitting along the δ/γ interface, while inside the δ phase, a selective corrosion occurred due to the low potential of ferrite phase.

4 Conclusion

The effect of aging time on the precipitation morphology and the interface evolution of LDX 2101 stainless steel have been investigated using SEM, AFM, and nano-indentation measurements. The following conclusions can be drawn:

- Needle-like structures of Cr_2N nitrides with 200 nm of length are precipitated at the earliest stages of aging that grow to 2 μm in length after 24 h of aging at 750 °C.
- After 10 min of aging, triangular $Cr_{23}C_6$ carbides are detected only along the δ/γ interface with 150-nm main size while Cr_2N nitrides start to precipitate after long term of aging (120 h) along the δ/δ interface.
- The high precipitation content of Cr_2N results in the increase of the δ/γ interface nano-hardness with aging time while the δ/δ interface remains unaffected by aging treatment.
- Increasing the aging time to 240 h results in the worst surface aspect, which presents deep pits of 30 nm in depth and high surface imperfection at the grain boundaries.
- Selective corrosion occurred into the δ phase and around the Cr_2N nitrides where the γ_2 phase acts as the origin of pitting along the δ/γ interface.

Availability of data and material The authors confirm that the data supporting the findings of this study are available within the article. The raw data that support the findings of this study are available upon reasonable request.

Code availability Not applicable.

Declarations

Ethical approval This study complies with the ethical standards set out by Springer. All the authors read and approved the final manuscript.

Conflict of interest The authors declare no competing interests.

References

1. Tehovnik F, Batič BŠ, Vode F et al (2018) Nitrides and carbides in 2101 lean duplex stainless steel. Mater Tehnol 52:821–826. https://doi.org/10.17222/mit.2018.145
2. Ran Q, Xu Y, Li J, Wan J, Xiao X, Yu H, Jiang L (2014) Effect of heat treatment on transformation-induced plasticity of economical Cr19 duplex stainless steel. Mater Des 56:959–965. https://doi.org/10.1016/j.matdes.2013.12.019
3. Choi JY, Ji JH, Hwang SW, Park KT (2012) TRIP aided deformation of a near-Ni-free, Mn-N bearing duplex stainless steel. Mater Sci Eng A 535:32–39. https://doi.org/10.1016/j.msea.2011.12.037
4. Breda M, Pellizzari M, Frigo M (2015) σ-Phase in lean duplex stainless steel sheets. Acta Metall Sin (Engl Lett) 28:331–337. https://doi.org/10.1007/s40195-014-0201-9
5. Silva R, Baroni LFS, Silva MBR, Afonso CRM, Kuri SE, Rovere CAD (2016) Effect of thermal aging at 475 ° C on the properties of lean duplex stainless steel 2101. Mater Charact 114:211–217. https://doi.org/10.1016/j.matchar.2016.03.002
6. Calliari I, Pellizzari M, Zanellato M, Ramous E (2011) The phase stability in Cr-Ni and Cr-Mn duplex stainless steels. J Mater Sci 46:6916–6924. https://doi.org/10.1007/s10853-011-5657-7
7. Liljas M, Johansson P, Liu H-P, Olsson C-OA (2008) Development of a lean duplex stainless steel. Steel Res Int 79:466–473. https://doi.org/10.1002/srin.200806154
8. Maetz J, Cazottes S, Verdu C, Kleber X (2015) Precipitation and phase transformations in 2101 lean duplex stainless steel during isothermal aging. Metall Mater Trans A 47:239–253. https://doi.org/10.1007/s11661-015-3215-7
9. Lee KM, Cho H, Choi DC (1999) Effect of isothermal treatment of SAF 2205 duplex stainless steel on migration of δ/γ interface boundary and growth of austenite. J Alloys Compd 285:156–161. https://doi.org/10.1016/S0925-8388(99)00014-6
10. Zhang W, Jiang LZ, Gao JQ, Song HM, Hu JC (2010) Study of precipitation in 2101 duplex stainless steel. Mater Sci Technol 26:515–521. https://doi.org/10.1179/174328409X405689
11. Zelinka SL, Ortiz-candelaria L, Rammer DR (2009) Electrochemical impedance spectroscopy (EIS) as a tool for measuring corrosion of polymer-coated fasteners used in treated wood. For Prod J 59:77–82
12. Ze W, Jianxin D, Youqiang X et al (2012) Effect of surface texturing on friction properties of WC / Co cemented carbide. Mater Des 41:142–149. https://doi.org/10.1016/j.matdes.2012.05.012
13. Ouali N, Khenfer K, Belkessa B, Fajoui J, Cheniti B, Idir B, Branchu S (2019) Effect of heat input on microstructure, residual stress, and corrosion resistance of UNS 32101 lean duplex stainless steel weld joints. J Mater Eng Perform 28:4252–4264. https://doi.org/10.1007/s11665-019-04194-w
14. Ahn S, Kang S (2000) Formation of core / rim structures in Ti (C , N) -WC-Ni cermets via a dissolution and pricipitation process. J Am Ceram Soc 83:1489–1494. https://doi.org/10.1111/j.1151-2916.2000.tb01415.x
15. Sieurin H, Sandström R, Westin EM (2006) Fracture toughness of the lean duplex stainless steel LDX 2101. Metall Mater Trans A Phys Metall Mater Sci 37:2975–2981. https://doi.org/10.1007/s11661-006-0179-7
16. Atapour M, Sarlak H, Esmailzadeh M (2016) Pitting corrosion susceptibility of friction stir welded lean duplex stainless steel joints.

Int J Adv Manuf Technol 83:721–728. https://doi.org/10.1007/s00170-015-7601-5
17. Sathirachinda N, Pettersson R, Wessman S, Pan J (2010) Study of nobility of chromium nitrides in isothermally aged duplex stainless steels by using SKPFM and SEM/EDS. Corros Sci 52:179–186. https://doi.org/10.1016/j.corsci.2009.08.057
18. Nilsson JO, Wilson A (1993) Influence of isothermal phase transformations on toughness and pitting corrosion of super duplex stainless steel SAF 2507. Mater Sci Technol (UK) 9:545–554. https://doi.org/10.1179/mst.1993.9.7.545
19. Wei Z, Laizhu J, Jincheng H, Hongmei S (2009) Effect of ageing on precipitation and impact energy of 2101 economical duplex stainless steel. Mater Charact 60:50–55. https://doi.org/10.1016/j.matchar.2008.07.002
20. Maamache B, Cheniti B, Belkessa B, Tahar-chaouch K, Kouba R (2021) Effect of aging temperature on the microstructure, local mechanical properties, and wear behavior of a UNS S32750 super duplex stainless steel. J Mater Eng Perform 30:546–555. https://doi.org/10.1007/s11665-020-05332-5
21. Zhang Z, Zhao H, Zhang H, Yu Z, Hu J, He L, Li J (2015) Effect of isothermal aging on the pitting corrosion resistance of UNS S82441 duplex stainless steel based on electrochemical detection. Corros Sci 93:120–125. https://doi.org/10.1016/j.corsci.2015.01.014
22. Sathirachinda N, Pettersson R, Wessman S, Kivisäkk U, Pan J (2011) Electrochimica Acta Scanning Kelvin probe force microscopy study of chromium nitrides in 2507 super duplex stainless steel — implications and limitations. Electrochim Acta 56:1792–1798. https://doi.org/10.1016/j.electacta.2010.08.038
23. Deng B, Wang Z, Jiang Y, Wang H, Gao J, Li J (2009) Evaluation of localized corrosion in duplex stainless steel aged at 850 ° C with critical pitting temperature measurement. Electrochim Acta 54:2790–2794. https://doi.org/10.1016/j.electacta.2008.11.038
24. Deng B, Jiang YM, Gao J, Li J (2010) Effect of annealing treatment on microstructure evolution and the associated corrosion behavior of a super-duplex stainless steel. J Alloys Compd 493:461–464. https://doi.org/10.1016/j.jallcom.2009.12.127
25. Garfias-Mesias LF, Sykes JM, Tuck CDS (1996) The effect of phase compositions on the pitting corrosion of 25 Cr duplex stainless steel in chloride solutions. Corros Sci 38:1319–1330
26. Perren RA, Suter T, Solenthaler C, Gullo G, Uggowitzer PJ, Böhni H, Speidel MO (2001) Corrosion resistance of super duplex stainless steels in chloride ion containing environments: investigations by means of a new microelectrochemical method. II. Influence of precipitates. Corros Sci 43:727–745. https://doi.org/10.1016/S0010-938X(00)00088-3
27. Ha HY, Kwon HS (2007) Effects of Cr2N on the pitting corrosion of high nitrogen stainless steels. Electrochim Acta 52:2175–2180. https://doi.org/10.1016/j.electacta.2006.08.034
28. Oliver WC, Pharr GM (1992) An improved technique for determining hardness and elastic modulus using load and displacement sensing indentation experiments. J Mater Res 7:1564–1583
29. Zhao Y, Wang Y, Li X, Zhang W, Tang S, Liu Z (2018) Effects of plastic straining on the corrosion resistance of TRIP-aided lean duplex stainless steels. J Mater Sci 53:9258–9272. https://doi.org/10.1007/s10853-018-2196-5
30. Zhang L, Zhang W, Jiang Y, Deng B, Sun D, Li J (2009) Electrochimica Acta Influence of annealing treatment on the corrosion resistance of lean duplex stainless steel 2101. Electrochim Acta 54:5387–5392. https://doi.org/10.1016/j.electacta.2009.04.023
31. Chan KW, Tjong SC (2014) Effect of secondary phase precipitation on the corrosion behavior of duplex stainless steels. Materials 7:5268–5304. https://doi.org/10.3390/ma7075268
32. Simmons JW (1996) Overview: High-nitrogen alloying of stainless steels. Mater Sci Eng A 207:159–169. https://doi.org/10.1016/0921-5093(95)09991-3
33. Deng B, Jiang Y, Xu J, Sun T, Gao J, Zhang L, Zhang W, Li J (2010) Application of the modified electrochemical potentiodynamic reactivation method to detect susceptibility to intergranular corrosion of a newly developed lean duplex stainless steel LDX2101. Corros Sci 52:969–977. https://doi.org/10.1016/j.corsci.2009.11.020
34. Maetz JY, Douillard T, Cazottes S, Verdu C, Kléber X (2016) M23C6 carbides and Cr2N nitrides in aged duplex stainless steel: a SEM, TEM and FIB tomography investigation. Micron 84:43–53. https://doi.org/10.1016/j.micron.2016.01.007
35. Hong HU, Rho BS, Nam SW (2001) Correlation of the M23C6 precipitation morphology with grain boundary characteristics in austenitic stainless steel. Mater Sci Eng A 318:285–292. https://doi.org/10.1016/S0921-5093(01)01254-0
36. Silva IC, Rebello JMA, Bruno AC et al (2008) Structural and magnetic characterization of a carburized cast austenitic steel. Scr Mater 59:1010–1013. https://doi.org/10.1016/j.scriptamat.2008.07.015
37. Stevens KJ, Parbhu A, Soltis J, Stewart D (2003) Magnetic force microscopy of a carburized ethylene pyrolysis tube. J Phys D Appl Phys 36:164–168. https://doi.org/10.1088/0022-3727/36/2/315
38. Zhao Y, Zhang W, Liu Z, Wang G (2017) Development of an easy-deformable Cr21 lean duplex stainless steel and the effect of heat treatment on its deformation mechanism. Mater Sci Eng A 702:279–288. https://doi.org/10.1016/j.msea.2017.07.020
39. Fang YL, Liu ZY, Xue WY, Song HM, Jiang LZ (2010) Precipitation of secondary phases in lean duplex stainless steel 2101 during isothermal ageing. ISIJ Int 50:286–293. https://doi.org/10.2355/isijinternational.50.286
40. Guo LQ, Li M, Shi XL, Yan Y, Li XY, Qiao LJ (2011) Effect of annealing temperature on the corrosion behavior of duplex stainless steel studied by in situ techniques. Corros Sci 53:3733–3741. https://doi.org/10.1016/j.corsci.2011.07.019